 SDHM, vol.3, no.2, pp.107-119, 2007

Meshless Method with Enriched Radial Basis Functions for Fracture Mechanics

P.H. Wen[1] **and M.H. Aliabadi**[2]

Abstract: In the last decade, meshless methods for solving differential equations have become a promising alternative to the finite element and boundary element methods. Based on the variation of potential energy, the element-free Galerkin method is developed on the basis of finite element method by the use of radial basis function interpolation. An enriched radial basis function is formulated to capture the stress singularity at the crack tip. The usual advantages of finite element method are retained in this method but now significant improvement of accuracy. Neither the connectivity of mesh in the domain by the finite element method or integrations with fundamental/particular solutions by the boundary element method is required in this approach. The applications of element-free Galerkin method with enriched radial basis function for two-dimensional fracture mechanics have been presented and comparisons have been made with benchmark analytical solutions.

Keyword: Element-free Galerkin method, Variation of potential energy, Cracks, Enriched radial base function, Stress intensity factors.

1 Introduction

Engineering computations have made significant progress over the past three decades and the most successful methods among them are the finite element method and the boundary element method. It is well-known that the finite element method (FEM) is the most widely used numerical method which can effectively deal with linear, nonlinear and large scale problems. However, the finite element method suffers from drawbacks of requiring the generation of a mesh cells with thousands of nodes, particularly for the crack propagation and moving boundaries. The boundary element method (BEM) is now a well-established technique for analysis of certain engineering problem with particular advantages. But many integrals over the domain occur in the boundary integral equations for most nonlinear problems. Moreover, pure boundary integral formulations are available only if the fundamental solution of the governing operator is known.

Meshless approximations have received much interest since Nayroles *et al* (1992) proposed the diffuse element method. Later, Belyschko *et al* (1994) and Liu *et al* (1995) proposed element-free Galerkin method (EFGM) and reproducing kernel particle methods, respectively. A key feature of these methods is that they do not require a structured grid and are hence meshless. Recently, Atluri and co-workers presented a family of Meshless methods, based on the Local weak Petrov-Galerkin formulation (MLPGs) for arbitrary partial differential equations [S.N. Atluri *et al* (1998a, 1998b, 1999, 2002, 2004)] with moving least-square (MLS) approximation. MLPG is reported to provide a rational basis for constructing meshless methods with a greater degree of flexibility. Local Boundary Integral Equation (LBIE) with moving least square and polynomial radial basis function (RBF) has been developed by Sladek *et al* (2004, 2005, 2006) for the boundary value problems in anisotropic non-homogeneous media. Both methods (MLPG and LBIE) are meshless, as no domain/boundary meshes are required in these two approaches. However, Galerkin-base meshless methods, except MLGP presented by Atluri (2004) still include several awkward implementation features such as numer-

[1] Department of Engineering, Queen Mary, University of London, London, UK, E1 4NS.
[2] Department of Aeronautics, Imperial College, London, UK, SW7 2BY.

ical integrations in the local domain. A comprehensive review of meshless methods (MLPG) can be found in the book [Atluri (2004)] by Atluri.

A range of local interpolation schemes that interpolate the randomly scattered points is currently available. The moving least square and radial basis function interpolations are two popular approximation techniques recently developed. Comparisons of these two techniques have shown that the moving least-square approximation is the generally best scheme with a reasonable accuracy Wen *et al* (2007). Lancaster and Salkauskas (1981) present the properties of MLS approximation in details. Moreover, the development of the radial basis function interpolation as a truly meshless method has drawn the attention of many investigators (see Golberg *et al* (1996)). Hardy (1971), Kansa (1991a, 1991b) Hon *et al* (1997) used multiquadric interpolation method for solving spatial approximation scheme for parabolic, hyperbolic and the elliptic Poisson's equationlinear differential equation. Li *et al* (2003) compared two meshless methods, i.e. the method of fundamental solution (MFS) and dual reciprocity method (DRM), by the use of radial basis functions. Numerical results indicate that these two methods provide a similar optimal accuracy in solving both 2D Poisson's and parabolic equations.

Using the finite element method, we calculate the displacements and stresses in each element by its nodal values of displacement. In addition, the material properties such as Young's modulus and Poisson ratio are treated as constants in each element. Apparently the stresses are not continuous crossing each element, although the displacements are continuous everywhere. Hence, these discontinuities of stress and material properties in the field reduce the accuracy of numerical simulation. For instance, to achieve high accuracy around a sharp corner or in front of the crack tips, high density elements or special elements must be introduced in the local region by FEM. The application of meshless method to fracture mechanics, i.e. evaluation of stress intensity factors at crack tips and analysis of crack growth, were demonstrated by Fleming *et al* (1997) and Rao *et al* (2001) by using enriched basis function in the moving least square interpolation. However, this method is computationally expensive because a coefficient matrix must be inverted at each Gauss integration point. In this paper, a element free Galerkin method is presented with compactly supported enriched radial basis function (RBF) interpolation. Following the same technique to derive system equations for finite element method, the stiffness matrix is established by the variation of potential energy using enriched RBF interpolations. Therefore, the stiffness matrix is still symmetric and has a diagonal strip distribution and also this method can be combined with FEM directly. The accuracy of proposed method has been demonstrated through benchmark examples.

2 Variation of potential energy

In the case of a homogeneous anisotropic and linear elasticity, relationship between the stress and strain by Hooke's law can be written as

$$\sigma_{ij}(\mathbf{x}) = C_{ijkl}(\mathbf{x})\varepsilon_{kl}(\mathbf{x}) = C_{ijkl}(\mathbf{x})u_{k,l}(\mathbf{x}), \tag{1}$$

where $\varepsilon_{kl} = (u_{k,l} + u_{l,k})/2$, and C_{ijkl} denotes the elasticity tensor which has the following symmetries

$$C_{ijkl} = C_{jikl} = C_{klij}. \tag{2}$$

For a homogeneous isotropic solid, we have

$$C_{ijkl}(\mathbf{x}) = \lambda(\mathbf{x})\delta_{ij}\delta_{kl} + \mu(\mathbf{x})\left(\delta_{ik}\delta_{jl} + \delta_{il}\delta_{jk}\right) \tag{3}$$

where λ and μ are the Lame's constants. For the isotropic plane stress state, Hooke's law can also be written, in matrix form, as

$$\boldsymbol{\sigma} = \begin{Bmatrix} \sigma_{11} \\ \sigma_{11} \\ \sigma_{11} \end{Bmatrix} = \mathbf{D} \begin{Bmatrix} \varepsilon_{11} \\ \varepsilon_{22} \\ \varepsilon_{12} \end{Bmatrix} = \mathbf{D}\boldsymbol{\varepsilon} \tag{4}$$

where

$$\mathbf{D} = \frac{E}{1-\nu^2} \begin{bmatrix} 1 & \nu & 0 \\ \nu & 1 & 0 \\ 0 & 0 & \frac{1-\nu}{2} \end{bmatrix} \tag{5}$$

in which, E is the Young's modulus and ν the Poisson's ratio. Consider the domain Ω enclosed

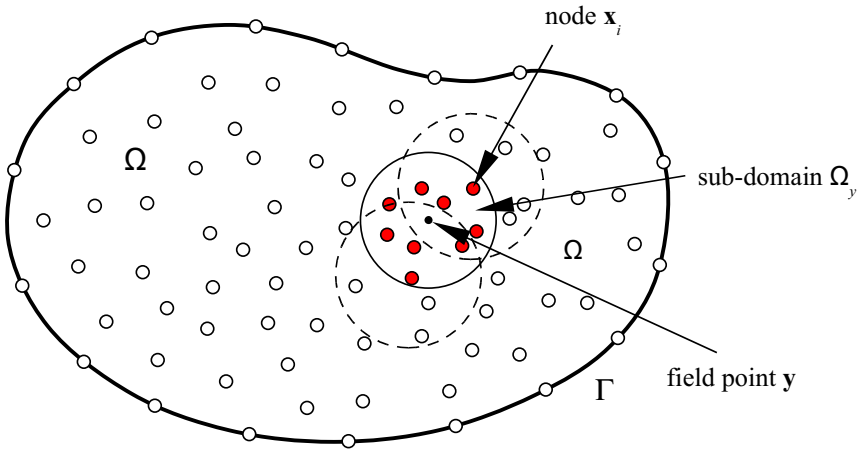

Figure 1: Sub-domain Ω_y for RBF interpolation of the field point $\mathbf{y}$ and support domains.

by boundary $\tilde{\mathrm{A}}$, we have the total potential energy for the plane stress by

$$\Pi = U - W \tag{6}$$

where the initial elastic strain energy

$$U = \frac{1}{2}\int_{\Omega} \boldsymbol{\sigma}^{\mathrm{T}}(\mathbf{y})\boldsymbol{\varepsilon}(\mathbf{y})d\Omega(\mathbf{y}) = \frac{1}{2}\int_{\Omega} \boldsymbol{\varepsilon}^{\mathrm{T}}(\mathbf{y})\mathbf{D}\boldsymbol{\varepsilon}(\mathbf{y})d\Omega(\mathbf{y}) \tag{7}$$

and the external energy, the sum of contributions from known interior and boundary forces, is

$$W = \int_{\Omega} \mathbf{u}^{\mathrm{T}}(\mathbf{y})\mathbf{b}(\mathbf{y})d\Omega(\mathbf{y}) + \int_{\Gamma} \mathbf{u}^{\mathrm{T}}(\mathbf{y})\mathbf{t}(\mathbf{y})d\Gamma(\mathbf{y}) \tag{8}$$

where $\mathbf{b} = \{b_1, b_2\}^{\mathrm{T}}$ is the body force vector, $\mathbf{t} = \{t_1, t_2\}^{\mathrm{T}}$ in which $t_i = \sigma_{ij}n_j$, the vector of traction on the boundary and n_i denotes a unit outward normal vector. We assume that the displacements $\mathbf{u}(\mathbf{y})$ at the point $\mathbf{y}$ can be approximated in terms of the nodal values in a local domain (see Figure 1) as

$$u_i(\mathbf{y}) = \sum_{k=1}^{n(\mathbf{y})} \phi_k(\mathbf{y},\mathbf{x}_k)\hat{u}_i^k = \hat{\boldsymbol{\Phi}}(\mathbf{y},\mathbf{x})\hat{\mathbf{u}}_i \tag{9}$$

where

$$\hat{\boldsymbol{\Phi}}(\mathbf{y},\mathbf{x}) = \left\{\phi_1(\mathbf{y},\mathbf{x}_1), \phi_2(\mathbf{y},\mathbf{x}_2), \ldots, \phi_{n(\mathbf{y})}(\mathbf{y},\mathbf{x}_{n(\mathbf{y})})\right\}$$

and

$$\hat{\mathbf{u}}_i = \left\{\hat{u}_i^1, \hat{u}_i^2, \ldots, \hat{u}_i^{n(\mathbf{y})}\right\}^{\mathrm{T}}, \quad i = 1,2$$

$\hat{u}_i(\mathbf{x})$ is the nodal values at point $\mathbf{x}_k = \left\{x_1^{(k)}, x_2^{(k)}\right\}$, $k = 1,2,\ldots,n(\mathbf{y}), \phi_k$ the shape function and $n(\mathbf{y})$ the total number of node in the local domain named as the supported domain. For the two dimensional plane stress case, we can re-arrange the above relation as follows

$$\begin{aligned}
&\mathbf{u}(\mathbf{y}) = \{u_1, u_2\}^{\mathrm{T}} = \boldsymbol{\Phi}(\mathbf{y},\mathbf{x})\hat{\mathbf{u}} \\
&\boldsymbol{\Phi}(\mathbf{y},\mathbf{x}) = \begin{bmatrix} \hat{\boldsymbol{\Phi}} & 0 \\ 0 & \hat{\boldsymbol{\Phi}} \end{bmatrix} \\
&\quad = \begin{bmatrix} \phi_1 & 0 & \phi_2 & 0 & \ldots & \phi_{n(\mathbf{y})} & 0 \\ 0 & \phi_1 & 0 & \phi_2 & \ldots & 0 & \phi_{n(\mathbf{y})} \end{bmatrix} \\
&\hat{\mathbf{u}} = \left\{\hat{u}_1^1, \hat{u}_2^1, \hat{u}_1^2, \hat{u}_2^2 \ldots, \hat{u}_1^{n(\mathbf{y})}, \hat{u}_2^{n(\mathbf{y})}\right\}^{\mathrm{T}}
\end{aligned} \tag{10}$$

Therefore, the relationship between strains and displacements is given by

$$\begin{aligned}
&\boldsymbol{\varepsilon}(\mathbf{y}) \\
&= \begin{bmatrix} \frac{\partial\phi_1}{\partial x} & 0 & \frac{\partial\phi_2}{\partial x} & 0 & \ldots & \frac{\partial\phi_{n(\mathbf{y})}}{\partial x} & 0 \\ 0 & \frac{\partial\phi_1}{\partial y} & 0 & \frac{\partial\phi_2}{\partial y} & \ldots & 0 & \frac{\partial\phi_{n(\mathbf{y})}}{\partial y} \\ \frac{\partial\phi_1}{\partial y} & \frac{\partial\phi_1}{\partial x} & \frac{\partial\phi_2}{\partial y} & \frac{\partial\phi_2}{\partial x} & \ldots & \frac{\partial\phi_{n(\mathbf{y})}}{\partial y} & \frac{\partial\phi_{n(\mathbf{y})}}{\partial x} \end{bmatrix} \hat{\mathbf{u}} \\
&= \mathbf{B}(\mathbf{y})\hat{\mathbf{u}}.
\end{aligned} \tag{11}$$

To arrive at the system equations in terms of nodal displacement, consider the variation of the total

potential energy, with respect to each nodal displacements, to give

$$\delta\Pi = \delta U - \delta W = 0 \tag{12}$$

Inserting the relations $\mathbf{u} = \mathbf{\Phi}\hat{\mathbf{u}}$, $\boldsymbol{\varepsilon} = \mathbf{B}\hat{\mathbf{u}}$ and $\boldsymbol{\sigma} = \mathbf{D}\boldsymbol{\varepsilon}$ into Eq. (12) yields $2 \times N$ linear algebraic equations in the global coordinate system:

$$[\mathbf{K}]_{2N\times 2N}\,\hat{\mathbf{u}}_{2\times N} = \mathbf{f}_{2\times N} \tag{13}$$

where N is the total number of node in the domain Ω. The stiffness matrix becomes:

$$\mathbf{K} = \int_{\Omega} \mathbf{B}^{\mathrm{T}}(\mathbf{x},\mathbf{y})\mathbf{D}(\mathbf{y})\mathbf{B}(\mathbf{x},\mathbf{y})d\Omega(\mathbf{y}) \quad \text{for nodes } \mathbf{x} = \mathbf{x}_i \quad i = 1,2,\ldots,N, \tag{14}$$

and nodal force vector is

$$\mathbf{f} = \int_{\Omega} \mathbf{\Phi}^{\mathrm{T}}(\mathbf{x},\mathbf{y})\mathbf{b}(\mathbf{y})d\Omega(\mathbf{y}) + \int_{\Gamma_\sigma} \mathbf{\Phi}^{\mathrm{T}}(\mathbf{x},\mathbf{y})\mathbf{t}(\mathbf{y})d\Gamma(\mathbf{y}) \tag{15}$$

where Γ_σ denotes the boundary on which the traction is given. For a concentrated force acting at the node i, we may determine the nodal force vector directly by

$$\mathbf{f}_i = \left\{F_1^i, F_2^i\right\}^{\mathrm{T}} \tag{16}$$

where F_1 and F_2 denote the values of concentrated forces at the node either on the boundary (external applied force) or in the domain (inner body force). Therefore, the distributed loads including boundary loads and body forces can be simplified to nodal forces in the same way as FEM, so that the domain and boundary integrals in Eq. (15) can be avoided. It is worth to notice that for the finite element method, displacements at point $\mathbf{y}$ can be approximated by the nodal values of its own element only, and the number of node to be involved in interpolation depends on the element type, for instance, 3 for triangle element and 4 for rectangular. From the interpolation point of view, the accuracy of MLS and RBF should be higher than that of the finite element method, due to more nodes being involved.

3 The approximation scheme

The multiquadric RBF was introduced by Hardy (1971) in 1971 for interpolation of topographical surfaces. In 1991 Kansa (1991a, 1991b) presented an enhanced multiquadrics scheme developed for spatial approximations. Since all radial basis functions are defined globally, the resulting matrix for interpolation is dense and can be ill-conditioned, particularly for a large number of interpolation points. It also poses serious stability problems and is computationally inefficient.

A sub-domain $\Omega_y$as shown in Figure 1 is the neighbourhood of a point $\mathbf{y}$ and is also called support domain to an arbitrary point $\mathbf{y}$. The distribution of function u in the sub-domain Ω_y over a number of randomly distributed notes $\{\mathbf{x}_i\}$, $i = 1,2,\ldots,n(\mathbf{y})$ can be interpolated, at the point $\mathbf{y}$, by

$$u(\mathbf{y}) = \sum_{i=1}^{n(\mathbf{y})} R_i(\mathbf{y},\mathbf{x}_i)a_i = \mathbf{R}^{\mathrm{T}}(\mathbf{y},\mathbf{x})\mathbf{a}(\mathbf{y}) \tag{17}$$

where $\mathbf{R}^{\mathrm{T}}(\mathbf{y},\mathbf{x}) = \{R_1(\mathbf{y},\mathbf{x}), R_2(\mathbf{y},\mathbf{x}),\ldots, R_{n(\mathbf{y})}(\mathbf{y},\mathbf{x})\}$ is the set of radial basis functions centred at the point $\mathbf{y}$, $\{a_k\}_{k=1}^{n(\mathbf{y})}$ are the unknown coefficients to be determined. To capture the singular stresses in front of the crack tip, the enriched radial basis function has been selected to be the following

$$R_k(\mathbf{y},\mathbf{x}) = R(\mathbf{y}-\mathbf{x}_k) + Q(\mathbf{y}) = \sqrt{c^2 + |\mathbf{y}-\mathbf{x}_k|^2} + \left(\beta + \sqrt{r}e^{-\alpha r}\right) \tag{18}$$

where $r = |\mathbf{y}-\mathbf{y}_c|$; α, β and c are three free parameters; $\mathbf{y}_c(y_1^{(c)}, y_2^{(c)})$ denotes the crack tip. Also we select $c = b$(b is specified length, such as the width of the rectangular plate or the radius of the circular disk) in this paper. From the interpolation strategy in Eq. (18) for RBF, a linear system for the unknowns coefficients $\mathbf{a}$ is obtained by

$$\mathbf{R}_0\mathbf{a} = \hat{\mathbf{u}} \tag{19}$$

where coefficient matrix

$$\mathbf{R}_0 = \begin{bmatrix} R_1(\mathbf{x}_1,\mathbf{x}_1) & R_2(\mathbf{x}_1,\mathbf{x}_2) & \ldots & R_{n(\mathbf{y})}(\mathbf{x}_1,\mathbf{x}_{n(\mathbf{y})}) \\ R_1(\mathbf{x}_2,\mathbf{x}_1) & R_2(\mathbf{x}_2,\mathbf{x}_2) & \ldots & R_{n(\mathbf{y})}(\mathbf{x}_2,\mathbf{x}_{n(\mathbf{y})}) \\ \vdots & \vdots & \ddots & \vdots \\ R_1(\mathbf{x}_{n(\mathbf{y})},\mathbf{x}_1) & R_2(\mathbf{x}_{n(\mathbf{y})},\mathbf{x}_2) & \ldots & R_{n(\mathbf{y})}(\mathbf{x}_{n(\mathbf{y})},\mathbf{x}_{n(\mathbf{y})}) \end{bmatrix}$$

(20)

As the RBFs are positive definite, the matrix $\mathbf{R}_0$ is assured to be invertible. Therefore, we can obtain the vector of unknowns from Eq. (19)

$$\mathbf{a} = \mathbf{R}_0^{-1}(\mathbf{x})\hat{\mathbf{u}}(\mathbf{x}) \tag{21}$$

So that the approximation $u(\mathbf{y})$ can be represented, at domain point $\mathbf{y}$, as

$$u(\mathbf{y}) = \mathbf{R}^{\mathrm{T}}(\mathbf{y},\mathbf{x})\mathbf{R}_0^{-1}(\mathbf{x})\hat{\mathbf{u}}(\mathbf{x}) = \hat{\mathbf{\Phi}}(\mathbf{y},\mathbf{x})\hat{\mathbf{u}} = \sum_{k=1}^{n(\mathbf{y})} \phi_k \hat{u}_k \tag{22}$$

where the nodal shape function are defined by

$$\hat{\mathbf{\Phi}}(\mathbf{y},\mathbf{x}) = \mathbf{R}^{\mathrm{T}}(\mathbf{y},\mathbf{x})\mathbf{R}_0^{-1}(\mathbf{x}) \tag{23}$$

It is worth noticing that the shape function depends uniquely on the distribution of scattered nodes within the support domain and has the property of Kronecker Delta. As the inverse matrix of coefficient $\mathbf{R}_0^{-1}(\mathbf{x})$ is a function only of distributed node $\mathbf{x}_i$ in the support domain, it is much simpler to evaluate the partial derivatives of shape function. From Eq. (22), we have

$$u_{,k}(\mathbf{y}) = \hat{\mathbf{\Phi}}_{,k}(\mathbf{y},\mathbf{x})\hat{\mathbf{u}} = \sum_{i=1}^{n(\mathbf{y})} \phi_{i,k}\hat{u}_i \tag{24}$$

where

$$\begin{aligned}\hat{\mathbf{\Phi}}_{,k}(\mathbf{y},\mathbf{x}) &= \mathbf{R}_{,k}^{\mathrm{T}}(\mathbf{y},\mathbf{x})\mathbf{R}_0^{-1}(\mathbf{x}) \\ &= [R_{1,k}(\mathbf{y},\mathbf{x}), R_{2,k}(\mathbf{y},\mathbf{x}), \ldots, R_{n(y),k}(\mathbf{y},\mathbf{x})]\mathbf{R}_0^{-1}(\mathbf{x})\end{aligned} \tag{25}$$

From Eq. (18), we have

$$\begin{aligned}R_{i,k}(\mathbf{y},\mathbf{x}_i) = &\frac{y_k - x_k^{(i)}}{\sqrt{c^2 + |\mathbf{y}-\mathbf{x}_i|^2}} \\ &+ \frac{y_k - y_k^{(c)}}{r}\left(\frac{1}{2\sqrt{r}} - \alpha\right) e^{-\alpha r}.\end{aligned} \tag{26}$$

Therefore, the displacement derivatives have $1/\sqrt{r}$ singularity near the crack tip.

4 Numerical process to evaluate stiffness matrix

To determine the stiffness matrix $\mathbf{K}$ in Eq.(13), a domain integral in Eq.(14) over the domain Ω should be carried out. For convenience of analysis, we assume that the domain can be divided into M rectangular sub-regions as shown in Figure 2 (for irregular shape of integral sub-domain, coordinate transformation, i.e. mapping technique, should be used). The 2D domain integral over a rectangular of area A is approximated by the Gaussian integration formula as

$$\iint_A f(x_1,x_2)dx_1dx_2 \approx A\sum_{l=1}^{L} w_l f(x_1^{(l)}, x_2^{(l)}) \tag{27}$$

where w_l denotes the weight of integral, L the

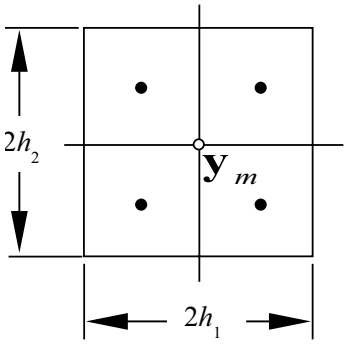

Figure 2: Gaussian integration points $\mathbf{y}_l(y_1^{(l)}, y_2^{(l)})$ for a two-dimensional problem.

number of Gaussian points and $(x_1^{(l)}, x_2^{(l)})$ is the coordinate of Gaussian points as shown in Figure 2. If domain Ω is divided into M sub-domain, then the matrix of stiffness can be written, using four Gaussian points scheme, as the following

$$\begin{aligned}\mathbf{K}(\mathbf{x}) &= \int_{\Omega} \mathbf{B}^{\mathrm{T}}(\mathbf{x},\mathbf{y})\mathbf{D}(\mathbf{y})\mathbf{B}(\mathbf{x},\mathbf{y})d\Omega(\mathbf{y}) \\ &= \sum_{m=1}^{M}\sum_{l=1}^{4} \frac{A_m}{4}\mathbf{B}^{\mathrm{T}}(\mathbf{x},\mathbf{y}_m^{(l)})\mathbf{D}(\mathbf{y}_m^{(l)})\mathbf{B}(\mathbf{x},\mathbf{y}_m^{(l)}) \\ &= \sum_{m=1}^{M}\sum_{l=1}^{4} \Delta\mathbf{K}_l^m\end{aligned} \tag{28}$$

where the integration points $\mathbf{y}_m^{(l)}(y_1^{(ml)}, y_2^{(ml)})$ and coefficients w_l are given by

$$\mathbf{y}_m^{(1,2,3,4)} = \left(y_1^m \pm \sqrt{\frac{1}{3}} h_1, y_2^m \pm \sqrt{\frac{1}{3}} h_2 \right), \quad w_{1,2,3,4} = \frac{1}{4}, \tag{29}$$

in which $\mathbf{y}_m(y_1^m, y_2^m)$ presents the centre of sub integral domain with area A_m (rectangular), h_1 and h_2 are half of the width and height of the rectangular region respectively and $A_m = 4h_1h_2$. For each Gaussian point $\mathbf{y}_l$, the elements in the stiffness sub-matrix $\Delta\mathbf{K}_l^m$ can be simplified to

$$\Delta\mathbf{K}_l^m = \frac{A_m E}{4(1-\nu^2)} \begin{bmatrix} \frac{\partial\phi_i}{\partial y_1}\frac{\partial\phi_j}{\partial y_1} + \frac{1-\nu}{2}\frac{\partial\phi_i}{\partial y_2}\frac{\partial\phi_j}{\partial y_2} & \nu\frac{\partial\phi_i}{\partial y_1}\frac{\partial\phi_j}{\partial y_2} + \frac{1-\nu}{2}\frac{\partial\phi_i}{\partial y_2}\frac{\partial\phi_j}{\partial y_1} \\ \nu\frac{\partial\phi_i}{\partial y_2}\frac{\partial\phi_j}{\partial y_1} + \frac{1-\nu}{2}\frac{\partial\phi_i}{\partial y_1}\frac{\partial\phi_j}{\partial y_2} & \frac{\partial\phi_i}{\partial y_2}\frac{\partial\phi_j}{\partial y_2} + \frac{1-\nu}{2}\frac{\partial\phi_i}{\partial y_1}\frac{\partial\phi_j}{\partial y_1} \end{bmatrix}_{ij} = \begin{bmatrix} a_{11}^l & a_{12}^l \\ a_{21}^l & a_{22}^l \end{bmatrix}_{ij} \tag{30}$$

where i and j denote the number of nodes in the local support domain centred at $\mathbf{y}_l$, $\phi_i = \phi_i(\mathbf{y}_l, \mathbf{x})$, $i, j = 1, 2, \ldots, n(\mathbf{y}_l)$. These four values in Eq. (30) should be added to the global system stiffness matrix $\mathbf{K}$, i.e. to the elements $k_{2I-1,2J-1}$, $k_{2I-1,2J}$, $k_{2I,2J-1}$ and $k_{2I,2J}$ respectively, as shown in the Figure 3, where I and J denote the numbers in the global system for the node i and j in the local support domain centred at $\mathbf{y}_l$. For each Gaussian point $\mathbf{y}_l$, the number of node i varies due to the change of centre of the support domain.

In the system stiffness matrix $\mathbf{K}$ in Eq. (28), the integral function has strong singularity of $O(1/r)$. Therefore, we need to use coordinate transformation technique to cancel that singularity for the integral sub region at the crack tip. For example, the sub region (two squares) is divided into four triangular sub domains and each triangular domain is transformed to a square as shown in Figure 4. The transformations are

- Triangular I: $y_1 = \xi_1$ and $y_2 = \frac{1}{2}[(1+\xi_1)\xi_2 - (1-\xi_1)]$; $J_c = \frac{1}{2}(1+\xi_1)$
- Triangular II: $y_1 = \frac{1}{2}[(1+\xi_1)\xi_2 - (1-\xi_1)]$ and $y_2 = \xi_1$; $J_c = \frac{1}{2}(1+\xi_1)$
- Triangular III: $y_1 = \frac{1}{2}[(1+\xi_2)\xi_1 + (1-\xi_2)]$ and $y_2 = \xi_2$; $J_c = \frac{1}{2}(1+\xi_2)$
- Triangular IV: $y_1 = -\xi_2$ and $y_2 = -\frac{1}{2}[(1+\xi_2)\xi_1 + (1-\xi_2)]$; $J_c = \frac{1}{4}(1+\xi_2)$

Thus, the integral with a strong singularity at $\mathbf{y}_c(-1,-1)$ can be written as

$$\begin{aligned} &\int_{-1}^{1}\int_{-1}^{1} \frac{F(y_1,y_2)}{r} dy_1 dy_2 \\ &= \int_{-1}^{1}\int_{-1}^{1} \frac{F(y_1,y_2)}{r} J_c^I(\xi_1) d\xi_1 d\xi_2 \\ &\quad + \int_{-1}^{1}\int_{-1}^{1} \frac{F(y_1,y_2)}{r} J_c^{II}(\xi_2) d\xi_1 d\xi_2 \\ &\quad + \int_{-1}^{1}\int_{-1}^{1} \frac{F(y_1,y_2)}{r} J_c^{III}(\xi_1) d\xi_1 d\xi_2 \\ &\quad + \int_{-1}^{1}\int_{-1}^{1} \frac{F(y_1,y_2)}{r} J_c^{IV}(\xi_2) d\xi_1 d\xi_2 \end{aligned} \tag{31}$$

where the Jacobian of transformation cancel out the $1/r$ singularity. This strong singularity was ignored in the work (1976, 2001) by the use of moving least square approximation and no discussion was presented on the accuracy of numerical calculation with ignoring such strong singularity.

Obviously the system stiffness matrix $\mathbf{K}$ is symmetric and has a diagonal strip distribution similar to the stiffness matrix of finite element method. As there are more nodes located in the local support domain than FEM, more accurate stress and strain (continuous) interpolations for stiffness matrix can be expected. The implementation of this method can be carried out according to the following routine, which is similar to the meshless method discussed by Atluri (2004):

(i) Choose a finite number of nodes N in the domain Ω and on the boundary $\tilde{\mathrm{A}}$ of the given physical domain; choose interpolation scheme such as MLS or RBF,

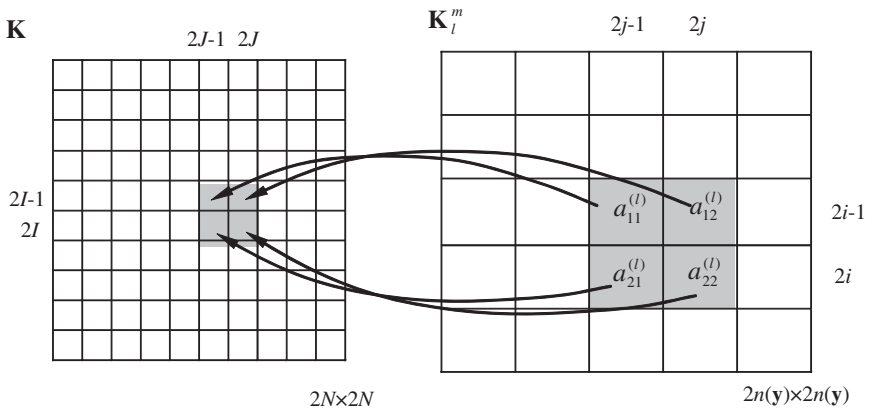

Figure 3: Stiffness matrix forming process, where i and j are node numbers in the support domain for integral Gaussian point l; I and J are numbers in the global system of nodes i and j.

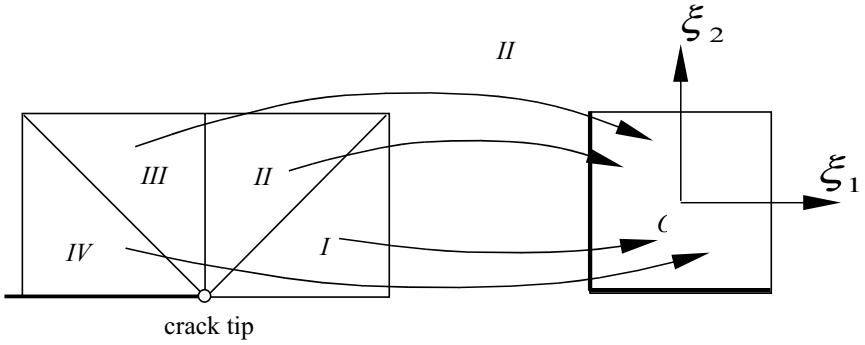

Figure 4: Transformation of triangle to square.

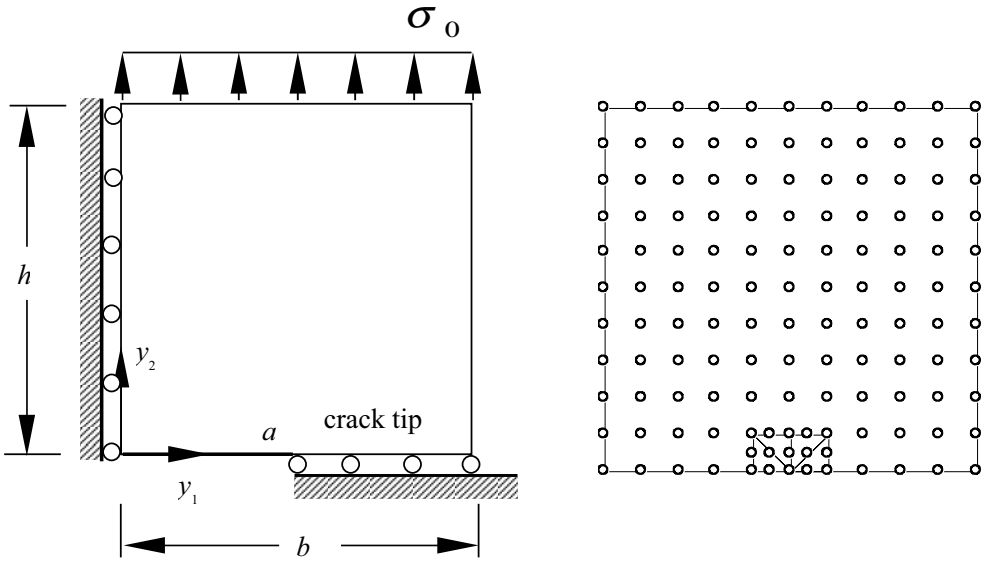

Figure 5: Square plate with a central crack ($h = b$) under tension σ_0: (a) a quarter of the plate; (b) uniformly distributed nodes.

(ii) Select the size and shape of local support domain or the minimum number in the support domain Ω_y

(iii) Divide domain Ω into segments and choose the shape of integral sub-domain

(iv) Loop over integral in sub domain m ($m = 1,2,\ldots,M$) centred at $\mathbf{y}_m$

- Loop over Gaussian integration points $\mathbf{y}_l$ (l=1,2,3,4) in the sub-domain,
  - (a) Loop over all nodes in the support domain (i, j);
    - i. Calculate the shape function $\phi_i(\mathbf{y}, \mathbf{x}_i)$ and first derivative $\phi_{i,k}(\mathbf{y}, \mathbf{x}_i)$;
  - (b) Evaluate the elements $\Delta\mathbf{K}_l^m = \left[a_{kl}^l\right]_{ij}$ with enrichment at crack tip;
    - i. Assemble the system stiffness matrix $\mathbf{K}_{(I,J)}$;
    - ii. End the node loop in the local domain,
- End the Gaussian point loop,

(v) End the sub-domain of integral loop,

(vi) Introduce the displacement boundary condition and modify the system equation,

(vii) Solve the linear equations for the nodal values,

(viii) Calculate the stresses and unknown variables by using the interpolations in the local support domain.

In addition, the width of the strip depends on the size of support domain or on the number of node in the support region. Therefore, the combination of element-free Galerkin method with finite element method can be realised easily. The stress intensity factors are evaluated by J-integral and crack opening displacement (COD) respectively. For mode I fracture, the stress intensity factor for plan stress problem is related to J-integral as following

$$K_I = \sqrt{EJ}$$
$$J = \int_\Gamma \left(W n_1 - t_\beta u_{\beta,1}\right) d\Gamma \tag{32}$$

where boundary Γ is an arbitrary contour surrounding the crack tip, n_α are the components of the outward normal to the contour and W denotes strain energy density, i.e.

$$W = \frac{1}{2}\sigma_{\alpha\beta}\varepsilon_{\alpha\beta}.$$

In this paper, a circle of radius r_0 centred at the crack tip is selected to be the J-integral contour. By the use of COD, the stress intensity factor is evaluated simply from

$$K_I = \frac{E}{8}\sqrt{\frac{2\pi}{r}}\Delta u_2, \quad \Delta u_2 = u_2^+ - u_2^-. \tag{33}$$

5 Numerical examples

5.1 A Single central crack in rectangular plate under tension

A square plate of width $2b$ and height $2h$ containing a central crack of length $2a$ is subjected to a uniform shear load σ_0 on the top and the bottom. Due to the symmetry, a quarter of plate is considered as shown in Figure 5 (a). Here Poisson's ratio ν=0.3 and Young's modulus is unit. A set of 11×11 ($N_{\text{total}} = 121$) uniformly distributed nodes is used and the integration is performed by dividing the square into 10×10 cells with 4×4 Gauss points in each cell in Figure 5 (b). Two cells near the crack tip need to be divided into four triangles for the strong singularity of integration at crack tip and 9×9 Gauss points for these triangular cells. The support domain is selected as a circle of radius d_y centered at field point $\mathbf{y}$, which is determined such that the minimum number of nodes in the sub domain $n(\mathbf{y}) \geq N_0$, here the number N_0 is selected to be 10 for all following examples. However, we found that for large number of support nodes in the sub-domain, the interpolation will become unstable for RBF interpolations due to the computational precision of

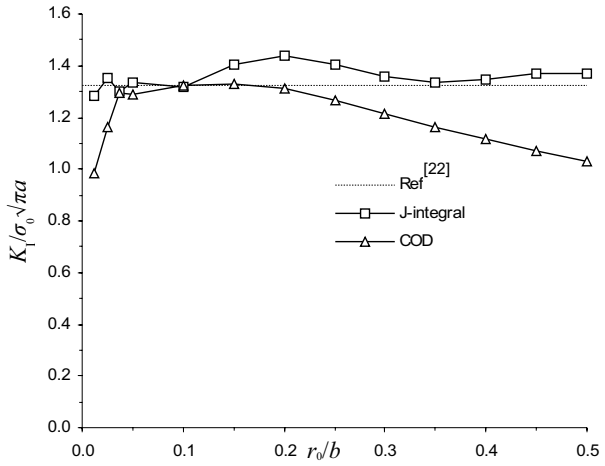

Figure 6: Normalized stress intensity factors vs. radius of J-integral contour or the distance for COD in square plate.

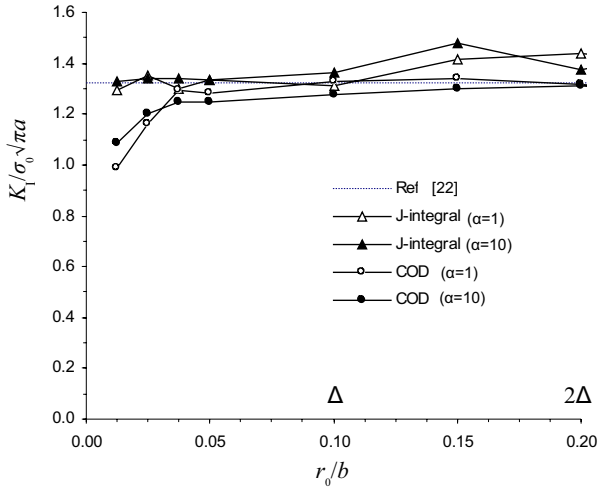

Figure 7: Normalized stress intensity factors vs. radius of J-integral contour or the distance for COD in square plate for different free parameter α when β=1.

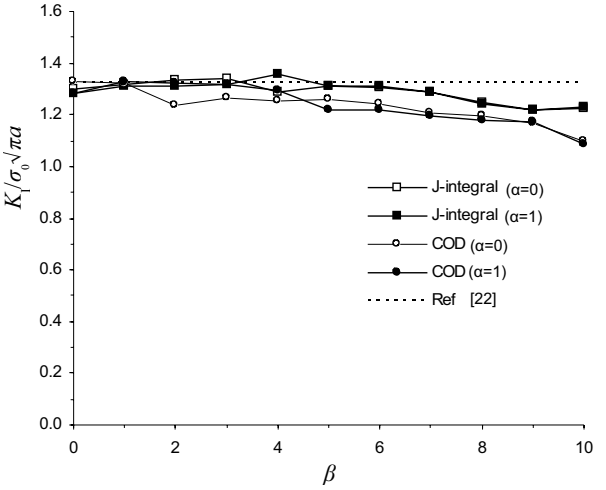

Figure 8: Normalized stress intensity factors vs. radius of J-integral contour or the distance for COD in square plate for different free parameter β.

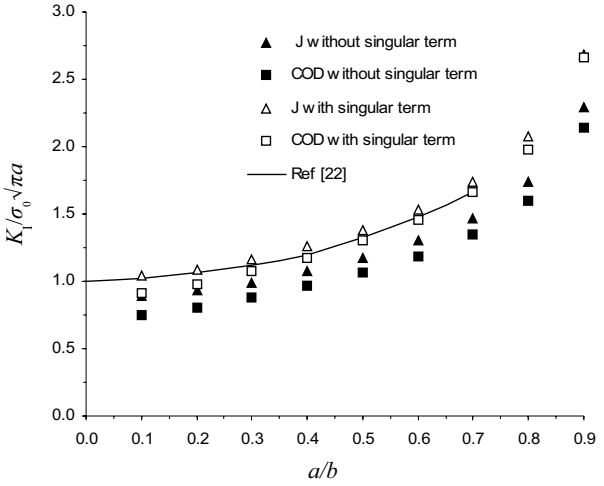

Figure 9: Comparison of normalized stress intensity factors with/without considering enriched singular term in RBFs when b/h=1.

FORTRAN. Figure 6 shows the sensitivity of the normalized stress intensity factor $K_I/\sigma_0\sqrt{\pi a}$ to the radius of J-integral contour or the distance between COD collocation point and crack tip r_0/b when the crack half-length $a = 0.5b$ and two free parameters $\alpha = \beta = 1$. It is evident that highly accurate solutions for both J-integral and COD techniques can be obtained when $r_0/\Delta = 1$, where Δ is the gap between two nodes, i.e. $0.1b$ in this case. The analytical solution for a square plate containing a central crack, if $a/b = 0.5$, is $K_I = 1.325\sigma_0\sqrt{\pi a}$[22]. Generally results obtained by J-integral are stable for the radius of integral contour. Therefore, in the following examples, the radius of integral contour for J-integral and distance for COD r_0 is selected as Δ. To study the sensitivity of numerical solution with different free parameter α, two values of α are examined. Figure 7 shows normalized stress intensity

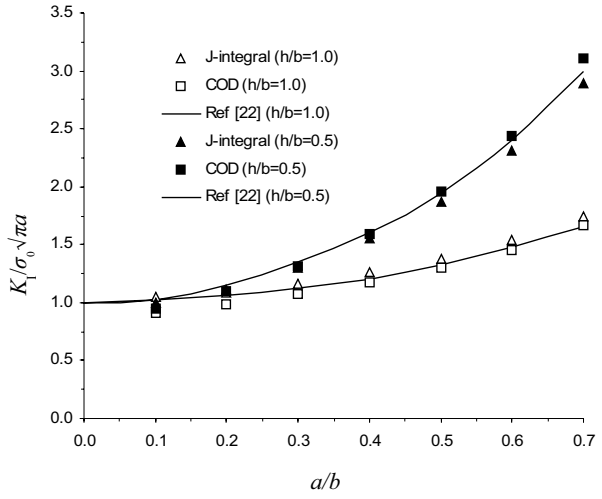

Figure 10: Normalized stress intensity factors for rectangular plate vs. ratio a/b when α=β=1.

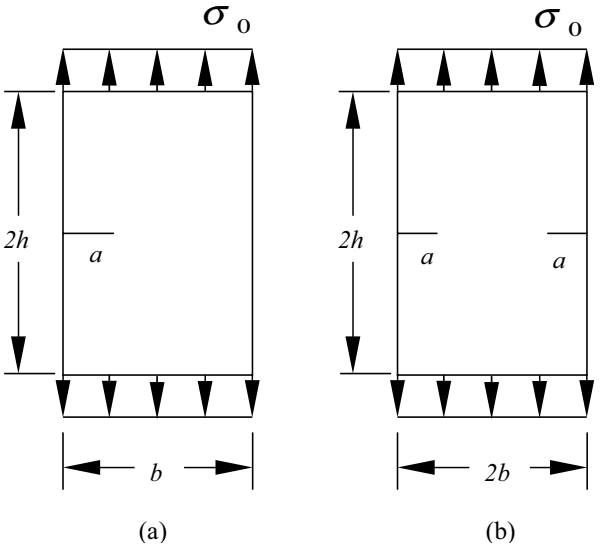

Figure 11: Geometry of rectangular plate with cracks: (a) edge crack; (b) symmetric double edge cracks.

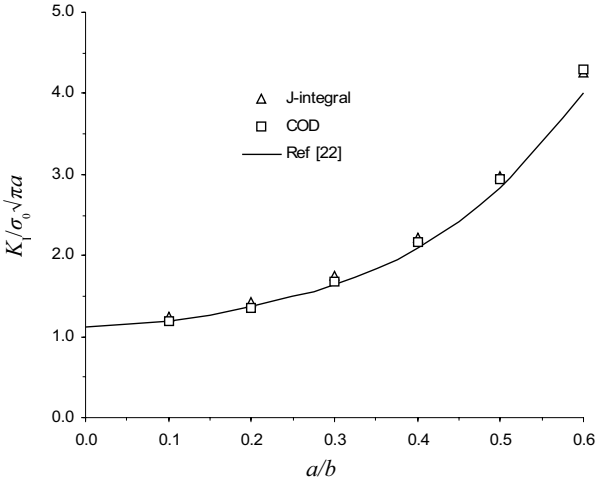

Figure 12: Normalized stress intensity factors for rectangular plate with edge crack vs. ratio a/b when α=β=1.

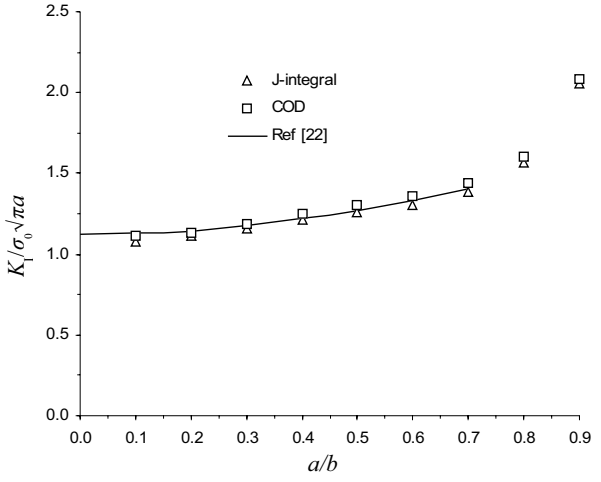

Figure 13: Normalized stress intensity factors for rectangular plate with double edge cracks vs. ratio a/b when α=β=1.

factors various with r_0 when $\alpha = 1$ and 10, respectively and $\beta = 1$. We found that the numerical solutions are quite stable for different values of parameter α and the relative error is less than 5%. In addition, the selection of parameter β is investigated in Figure 8 for $\alpha = 0$ and 1. Obviously the accuracy of solution is improved when $\alpha = 1$ and the more accurate results can be obtained for $0 < \beta < 4$ for both stress intensity factors evaluation techniques. Finally solutions with/without enriched term $Q(\sqrt{r})$ in the RBF interpolation are examined and are shown in Figure 9. We noticed that accuracy of solutions has been improved significantly by using enriched radial base function. In other words, the relative error without enriched singular term $Q(\sqrt{r})$ would be large than 20% for different crack length a/b. Furthermore, consider a rectangular plate b/h=2, a set of 21×11 uniformly distributed nodes is used and the integration is performed by dividing the square in

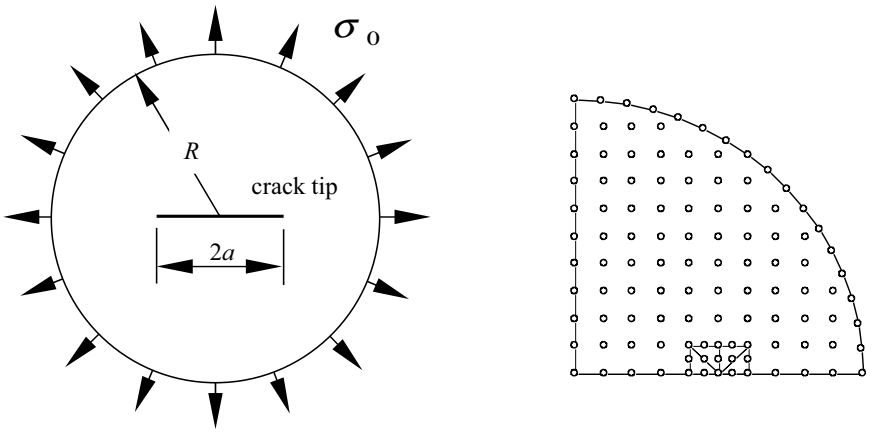

(a) (b)

Figure 14: A circular disk of radius R with a central crack of length $2a$ subjected to uniform load σ_0 on the boundary: (a) geometry; (b) distribution of nodes.

20×10 cells. Two free parameters $\alpha = \beta = 1$ and the radius of J-integral contour $r_0 = \Delta = 0.05b$. The normalize stress intensity factors by these two evaluation techniques are plotted in Figure 10. Good agreement with Reference [22] has been achieved.

5.2 Square plate with an edge and double edge cracks

In this example, a plate with an edge and symmetric double edge cracks as shown in Figure 11 (a) (b) is analysed respectively. Poisson's ratio ν=0.3 and density of node (21×21) is selected and thus, 441 nodes in total are uniformly distributed in the domain and on the boundary excluding 9 nodes in two special cells. The grid of sub-region for domain integral is selected as (20×20) and therefore sub-region number M=400. Uniform stress σ_0 is applied on the top and on the bottom of plate. Two free parameters $\alpha = \beta = 1$ and the radius of J-integral contour $r_0 = \Delta = 0.05b$ in this case. Figures 12 and 13 show the results of these examples. It can be seen that the present results are in good agreements with those presented in handbook by Rooke *et al* (1976) for edge/double edge crack problems respectively.

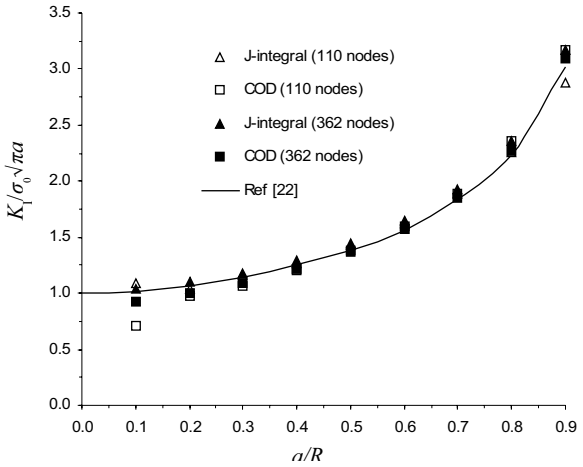

Figure 15: Comparison of normalized stress intensity factors of a circular disk containing a central crack for different number of nodes when α=β=1.

5.3 Circular disk with a central crack under tension

A circular disk of radius R containing a central crack of length $2a$ is subjected to a uniform tension σ_0 on the boundary as shown in Figure 14 (a). Poisson's ratio ν=0.3, Young's modulus is unit and quarter of disk as shown in Figure 14 (b) is analyzed. In this model, we have considered two densities of uniformly distributed nodes in the domain including 9 nodes in two special

cells near crack tip, i.e. N_{total}=110 and 362 respectively. Two free parameters $\alpha = \beta = 1$ and the radius of J-integral contour or the distance for COD $r_0 = \Delta$ in this case. Figure 15 shows the results of this example. In general, the present results are in good agreements with those presented in handbook by Rooke *et al* (1976). We also noticed that for small number of nodes and small crack half-length $a/b = 0.1$, the result given by COD technique is quite poor. It is because the collocation point is quite far away from crack tip relatively. However, J-integral method can produce high accurate solution. In the case of $a/b > 0.1$, both methods provide same accuracy of stress intensity factors.

6 Conclusion

It was demonstrated that by using enriched RBF interpolation in the local supported domain, we are able to capture the singular stresses $(1/\sqrt{r})$ at crack tip and to obtain more accurate solutions. The external boundary distributed load and internal body forces can be treated as concentrated forces in the same way as FEM. The computation of accurate stress intensity factors for two-dimensional mode I cracked structures were demonstrated by several examples. We can conclude with the following observations:

- The accuracy of SIFs can be improved significantly by using enriched RBF for two dimensional static elasticity;
- Enriched RBF is more flexible and simple to program than the moving least square interpolation, and less CPU time is required;
- This method is convergent similar to FEM;
- Similar to FEM, the stiffness matrix is ssymmetric and strip diagonal. Therefore, the coupling with FEM can be easily realised;
- The numerical solutions are stable for large range of free parameters selections.

In addition, for mixed mode fracture problem, it is more complicated to evaluate stress intensity factor using RBF.

References

Nayroles, B.; Touzot, G.; Villon, P. (1992): Generalizing the finite element method: diffuse approximation and diffuse elements, *Computational Mechanics*, 10, 307-318.

Atluri, S. N.; Zhu, T. (1998a): A new meshless local Peyrov-Galerkin (MLPG) approach to nonlinear problems in computational modelling and simulation, *Comput Model Simul Engng*, 3, 187-196.

Atluri, S. N.; Zhu, T. (1998b): A new meshless local Peyrov-Galerkin (MLPG) approach in computational mechanics, *Comput Mech*, 22, 117-127.

Atluri, S. N.; Zhu, T. (1999): The meshlesss local Peyrov-Galerkin (MLPG) approach for sovling problems in elasto-statics, *Comput Mech*, 25, 169-179.

Atluri, S. N.; Shen, S. (2002): The meshlesss local Peyrov-Galerkin (MLPG) method: a simple and less-costly alternative to the finite element and boundary element method, *CMES: Comput Model Engng Sci*, 3, 11-52.

Atluri, S. N. (2004): *The Meshless Method (MLPG) for Domain and BIE Discretizations*, Forsyth, GA, USA, Tech Science Press.

Belytschko, T.; Lu, Y. Y.; Gu, L. (1994): Element-free Galerkin method, *Int. J. Numerical Methods in Engineering*, 37, 229-256.

Golgerg, M. A.; Chen, C. S.; Karur, S. R. (1996): Improved multiquadric approximation for partial differential equations, *Engng Analy with Boundary Elements*, 18, 9-17, 1996.

Fleming, M.; Chu, Y. A.; Moran, B.; Belytschko, T.; Lu, Y. Y.; Gu, L. (1997): Enriched element-free Galerkin methods for crack-tip fields, *Int. J. Numerical Methods in Engineering*, 40, 1483-1504.

Hardy, R. L. (1971): Multiquadric equations of topography and other irregular surface, *J. Geophys. Res.*, 76, 1905-1915.

Hon, Y. C.; Mao, X. Z. (1997): A multiquadric interpolation method for solving initial value problems, *J. Scientific Computing*, 12, 51-55.

Kanse, E. J. (1991a): Multiquadrics. A scattered data approximation scheme with applications to computational fluid-dynamics. I. Surface approximations and partial derivative estimates, *Computer & Mathematics with Applications*, 19 (8-9), 127-145.

Kanse, E. J. (1991b): Multiquadrics. A scattered data approximation scheme with applications to computational fluid-dynamics. II. Surface Solutions to parabolic, hyperbolic and elliptic partial differential equations, *Computer & Mathematics with Applications*, 19 (8-9), 147-161.

Lancaster, P.; Salkauskas, K. (1981): Surfaces generated by moving least square methods, *Math Comp*, 37, 141-158.

Li, J.; Cheng, A. H.-D.; Chen, C.-S. (2003): A comparing of efficiency and error convergence of multiquadric collocation method and finite element method, *Engng Analy with Boundary Elements*, 27, 251-257.

Liu, W. K.; Jun, S.; Zhang, Y. (1995): Reproducing kernel particle methods, *Int. J. Numerical Methods in Engineering*, 20, 1081-1106.

Rao, B. N.; Rahman, S. A. (2001): Coupled meshless-finite element method for fracture analysis of cracks, *Int. J. Pressure Vessels and Piping*, 78, 647-657, 2001.

Rooke, D. P.; Cartwright, D. J. (1976): Compendium of Stress Intensity Factors, London, Her Majesty's Stationery Office.

Sladek, J.; Sladek, V.; Zhang, Ch. (2004): A meshless local boundary integral equation method for heat conduction analysis in nonhomogeneous solids, J. Chinese Institute Engng. 27, 517-539.

Sladek, J.; Sladek, V.; Wen, P. H.; Aliabadi, M. H. (2006): Meshless Local Petrov-Galerkin (MLPG) method for shear deformable shells analysis. *CMES: Computer Modeling in Engineering & Sciences*, 13, 103-117.

Sladek, J.; Sladek, V.; Tanaka M.; Zhang, Ch. (2005): Local integral equation method for potential problems in functionally graded anisotropic materials, *Engng Analy with Boundary Elements*, 29, 829-843.

Wen, P. H.; Aliabadi, M. H. (2007): An Improved Meshless Collocation Method for Elastostatic and Elastodynamic Problems, *Communications in Numerical Methods in Engineering*, (to appear).